Technical Note: Advances in flash flood monitoring using unmanned aerial vehicles (UAVs)

Matthew T. Perks, Andrew J. Russell, and Andrew R. G. Large

Newcastle University, School of Geography, Politics and Sociology, Daysh Building, Claremont Road,
Newcastle-upon-Tyne, NE1 7RU, UK

Correspondence to: M. T. Perks (matthew.perks@ncl.ac.uk)

Abstract. Unmanned aerial vehicles (UAVs) have the potential to capture information about the earth's surface in dangerous and previously inaccessible locations. Through image acquisition of flash flood events and subsequent object-based analysis, highly dynamic and oft-immeasurable hydraulic phenomena may be quantified at previously unattainable spatial and temporal resolutions. The potential for this approach to provide valuable information about the hydraulic conditions present during dynamic, high-energy flash floods has until now not been explored. In this paper we adopt a novel approach, utilizing the Kande–Lucas–Tomasi (KLT) algorithm to track features present on the water surface which are related to the free-surface velocity. Following the successful tracking of features, a method analogous to the vector correction method has enabled accurate geometric rectification of velocity vectors. Uncertainties associated with the rectification process induced by unsteady camera movements are subsequently explored. Geo-registration errors are relatively stable and occur as a result of persistent residual distortion effects following image correction. The apparent ground movement of immobile control points between measurement intervals ranges from 0.05 to 0.13 m. The application of this approach to assess the hydraulic conditions present in the Alyth Burn, Scotland, during a 1 : 200 year flash flood resulted in the generation of an average 4.2 at a rate of 508 measurements s^{-1}. Analysis of these vectors provides a rare insight into the complexity of channel–overbank interactions during flash floods. The uncertainty attached to the calculated velocities is relatively low, with a spatial average across the area of ± 0.15 m s^{-1}. Little difference is observed in the uncertainty attached to out-of-bank velocities (± 0.15 m s^{-1}), and within-channel velocities (± 0.16 m s^{-1}), illustrating the consistency of the approach.

1   Introduction

The occurrence of flash flooding from intense rainfall in western Europe is predicted to increase throughout the first half of the 21st century (Beniston, 2009; Rojas et al., 2012). These events pose severe risks to society, transform communities, and under extreme conditions can permanently alter the state of the river system (Doocy et al., 2013; Milner et al., 2013). Flash floods in fluvial systems pose high risks to communities, especially when they occur in small, upland catchments where orographic effects can enhance precipitation intensity with runoff being concentrated rapidly along narrow and steep flow pathways (Bracken and Croke, 2007; Sangati et al., 2009; Garambois et al., 2014). Despite a substantial body of work on physical flood processes observed in research catchments (e.g. Quinn and Beven, 1993; Soulsby et al., 2000; Mayes et al., 2006), there is currently a paucity of data describing the antecedent and concurrent processes associated with extreme flash flood events. This is mainly due to conventional monitoring networks often failing to adequately sample small, responsive catchments (Borga et al., 2008; Gaume and Borga, 2008; Soulsby et al., 2008; Braud et al., 2014). Measurement and monitoring of these events is therefore largely responsive rather than active, opportunistic rather than strategic, and hindered by practical difficulties (Borga et al., 2008; Tauro et al., 2015b). Making observations of peak flood discharge in real time remains a significant practical challenge.

Given current operational constraints, favourable sources of process data during flash floods in ungauged catchments often rely on post hoc analyses of air- and space-borne earth observation sensors (e.g. visible, near-infrared, and multispectral imaging and synthetic aperture radar). Increasing availability of these remotely sensed data has furthered our understanding of floodplain inundation processes (e.g. Wright et al., 2008); enabled hydraulic properties such as roughness (Simeonov et al., 2013), river stage, and discharge (Liu et al., 2015) to be successfully modelled; provided justification for the incorporation of spatially and temporally varied roughness values (Mason et al., 2003; Schumann et al., 2007); and enabled calibration and validation of hydrodynamic models (e.g. Martinis et al., 2009; Refice et al., 2014). Various contributions have been enabled by the fortuitous availability of archived satellite and aerial records (e.g. Chen and Mied, 2013; Kääb and Leprince, 2014). However, the highly transient temporal and spatial domains of flash floods, combined with the significant lead times required to mobilize monitoring resources, have up until now limited the use of satellite and aerial records to larger, more slowly responding catchments (e.g. Fujita and Kunita, 2011; Wong et al., 2015).

The widespread availability of unmanned aerial vehicles (UAVs) has, in recent years, increased our ability to monitor and quantify higher magnitude, and lower frequency environmental phenomena (e.g. Niethammer et al., 2012; Ryan et al., 2015), whilst at the same time reducing operational costs of traditional environmental monitoring (Fekete et al., 2015). The potential for the use of UAVs for non-contact flow measurement has been identified (Kääb and Leprince, 2014), leading to proof-of-concept studies utilizing UAVs for monitoring of low-flow conditions (e.g. Pagano et al., 2014; Detert and Weitbrecht, 2015; Patalano et al., 2015; Tauro et al., 2015a, b). However, the potential for this approach to provide valuable information about the hydraulic conditions present during dynamic, high-energy flash floods has yet to be realized.

Image-based non-contact methods of flow estimation utilize algorithms (e.g. Large-Scale Particle Tracking Velocimetry, LSPTV, and Large-Scale Particle Image Velocimetry, LSPIV) designed to track optically visible features of the free surface to determine the rate of fluid flow in artificial or natural open channels (Jodeau et al., 2008; Kim et al., 2008; Le Coz et al., 2010; Sun et al., 2010; Dramais et al., 2011; Puleo et al., 2012; Pentari et al., 2014; Le Boursicaud et al., 2015). The rate at which naturally occurring features (e.g. foam, seeds, woody debris, and turbulent structures) or artificially introduced tracers (e.g. Ecofoam chips, fluorescent micro-spheres) are displaced downstream can be used to estimate the free-surface velocity, which may be related to depth-averaged flow characteristics (e.g. Jodeau et al., 2008; Dramais et al., 2011; Fujita and Kunita, 2011; Simeonov et al., 2013; Le Boursicaud et al., 2015). Conceptually, terrestrial and airborne tracking of surface water features is similar; however, the uncertainties associated with rectification of captured images to account for perspective, radial, and tangential distortions are compounded when using a UAV for image acquisition. This is due to unsteady camera movement, which must be accounted for if accurate geometric rectification of velocity vectors or oblique images is to be achieved (Kantoush et al., 2008; Kim et al., 2008). A second source of uncertainty is introduced in situations where low seeding densities prevail, resulting in a lack of stable and identifiable surface features (Lewis and Rhoads, 2015). However, in the case of flash floods, coherent flow structures at the free surface and the presence of washed-in floating material may produce favourable seeding conditions (Jodeau et al., 2008; Dramais et al., 2011).

This paper presents a novel methodology for the derivation of key hydraulic data during flash floods using imagery captured by a low-cost, commercially available UAV platform. Our approach overcomes uncertainties associated with image rectification, transformation, and feature tracking to determine river surface velocity during flash floods. Our approach yields fundamental process data, invaluable for flash flood reconstruction in ungauged river catchments. The adoption of this technique has the potential to significantly advance our understanding of high-flow stage processes during flash floods.

2 Materials and methods

The materials presented in the following section describe the entire workflow for the extraction of surface water velocities from a UAV through the utilization of image-based non-contact methods. This method is organized in five subsections, which are presented sequentially: (i) primary data collection; (ii) development of an initial camera model, and (iii) updated camera models for projective transformations; (iv) assessment of transformation accuracy and apparent movement of GCPs; and, finally, (v) surface velocity calculation. A schematic overview of this method is provided in Fig. 1, wherein each heading corresponds to the homonymous section within the main text.

2.1 Primary data collection

On 17 July 2015, the Alyth Burn, Perthshire, Scotland (324600, 748600 OS BNG), breached its banks as a result of a prolonged period of rainfall over the catchment. While rainfall totals were not in themselves extreme (41 mm over a 6 h period), the prolonged nature of the precipitation event, coupled with the particular catchment configuration upstream of the town, resulted in over 70 properties being flooded and four footbridges in the town centre being destroyed (Perth and Kinross Council et al., 2015). During this flood event, a Phantom Vision 2 UAV equipped with a FC200 camera unit was deployed over the Alyth Burn in manual flight mode by
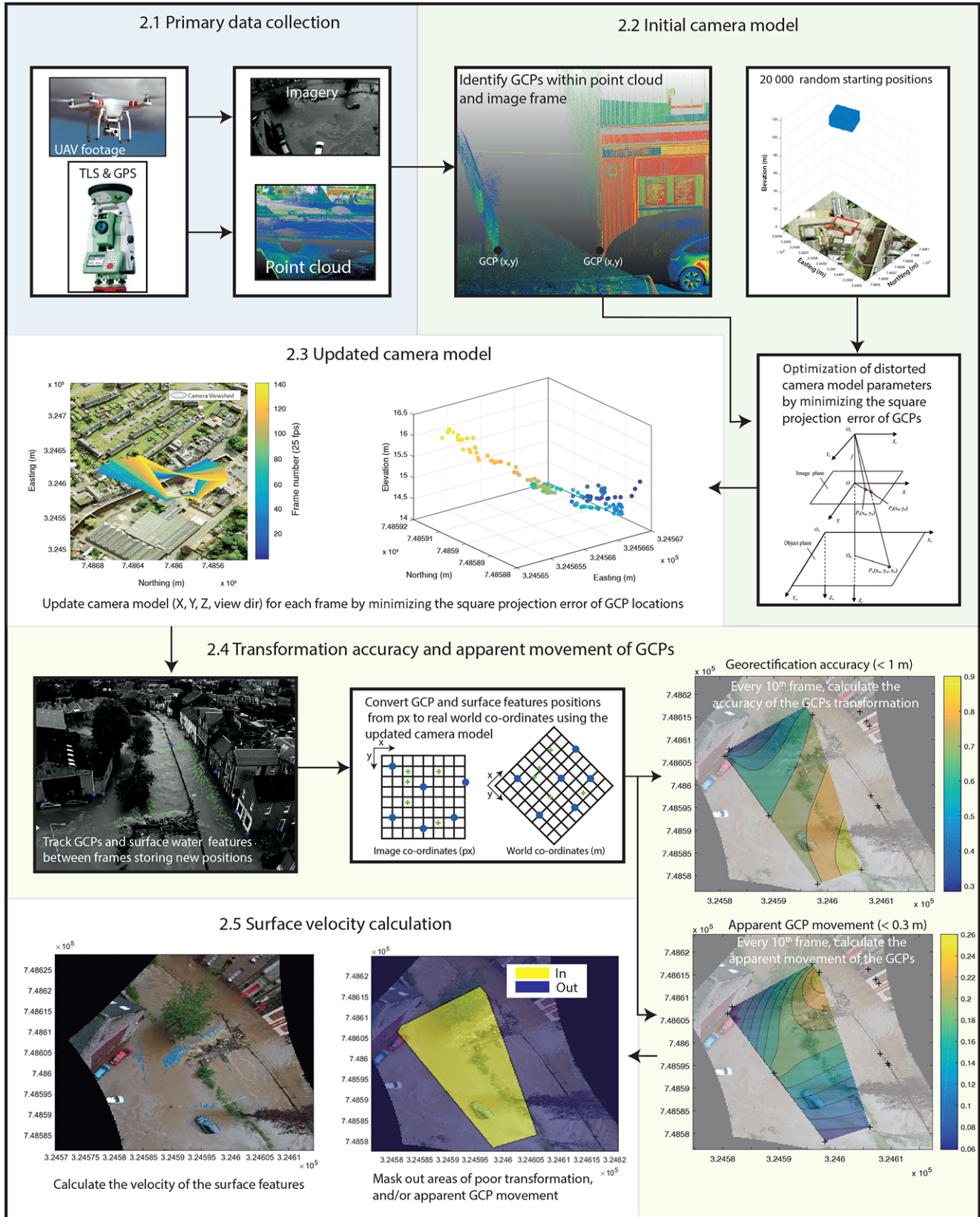
Figure 1. A schematic of the proposed methodology for tracking surface water features from UAVs and their conversion to velocities.

a member of the public at ~ 11:00 BST. The video footage itself was not collected with the intention of being used for flow reconstruction, but rather to document the impacts of the floods across the inundated area. Footage of the event was collected at 960×540 pixel (px) resolution at an acquisition rate of 25 frames per second (FPS).

Ground control points (GCPs) for the area of interest were required to convert the image (px) co-ordinates into geographical co-ordinates (OS BNG m). The deployment of a Leica MS50 multi-station shortly after the flood event enabled the generation of a detailed point cloud with an average point spacing of < 0.002 m from which GCPs could be accurately identified (Fig. 1, Sect. 2.1). These GCPs represented immobile objects that were present during the recording, and which persisted following the clean-up operation (e.g. lamp-posts and wall corners). Individual point clouds were joined using CloudCompare (2015), resulting in an internal error (RMS) of 0.04 m. This point cloud was rectified to real-world co-ordinates through comparison with control point measurements ($n = 12$) obtained by a Leica GS14 GNSS system. This resulted in an additional three-dimensional error of 0.06 m.

2.2 Initial camera model

Due to the lack of available navigation data for the UAV, its starting position was modelled using an a priori assumption about its approximate location $[X_{est}, Y_{est}, Z_{est}]$. This was based on a visual assessment of the objects within view of the camera; 20 000 co-ordinate solutions were randomly generated ($X_{est} \pm 7.5$ m; $Y_{est} \pm 7.5$ m; $Z_{est} \pm 5$ m), resulting in 8.9 discrete locations per m^3 (Fig. 1, Sect. 2.2). For each of these potential starting positions, a distorted camera model was generated in MATLAB 2016a (cf. Messerli and Grinsted, 2015). For each camera model, the radial distortion coefficients and image centre parameters that define the camera lens were fixed based on the manufacturer's specification. The focal length and view direction (yaw, pitch, and roll) were however free parameters and allowed to vary accordingly. These were optimized to minimize the square projection error of pre-determined GCPs using a modified Levenberg–Marquardt algorithm (Fletcher, 1971). The optimal solution was subsequently defined as the master camera model, which was used as the basis for future projective transformations.

2.3 Updated camera model

Following generation of the master camera model for the first frame of the video, an updated camera model solution based on updated GCP co-ordinates was generated for each subsequent frame (Messerli and Grinsted, 2015). This enabled UAV movement and changes in view direction to be accounted for. The updated camera model was obtained by randomly generating 1000 new camera positions proximal to the co-ordinates of the optimized camera model for the previous frame ($X \pm 0.25$; $Y \pm 0.25$; $Z \pm 0.25$ m). These camera co-ordinates were then fixed whilst the view direction was perturbed. The optimum camera model for each specific frame was produced by minimizing the difference between the actual and projected GCP co-ordinates. In order for this to be achieved, GCPs were defined and tracked iteratively between each frame using the Kande–Lucas–Tomasi (KLT) algorithm (Shi and Tomasi, 1994). Every tenth frame, the positions of existing GCPs were manually checked and their location manually updated when changes in illumination conditions resulted in poor tracking performance. Additional GCPs were also manually added to account for changes in the camera viewshed (Fig. 1, Sect. 2.3). This ensured that sufficient GCPs were visible throughout the video and that they were still accurately focussed on the object in question. All GCPs were level with the water surface, non-mobile, and clearly visible within the laser scan generated point cloud.

2.4 Transformation accuracy and apparent movement of GCPs

Every nth and $n + 9$th frame, where n equals the start of the tracking sequence, the start and finish positions of the successfully tracked GCPs were stored in pixel units representing motion during the previous 0.4 s of video. The start and finish positions of the GCPs (px) are converted to real-world coordinates $[N_T \, E_T]$ using a two-dimensional transformation (Fujita and Kunita, 2011; Fujita et al., 1998), based on the optimized camera models specific to the nth and $n + 9$th frames (Messerli and Grinsted, 2015). The degree to which the geo-rectification process is a success is assessed by comparing how the co-ordinates of the surveyed GCPs $[N, E]$ compare to the projected GCP locations $[N_T, E_T]$. The residuals $[r, s]$ represent the absolute positional error of the GCPs and provide a direct measure of the accuracy of the geometric transformation from pixel units into geographical co-ordinates (Fig. 1, Sect. 2.4), given by the Euclidean distance between the actual and projected locations R_{EN} (Detert and Weitbrecht, 2015):

$$[r, s] = [N_T, E_T] - [N, E], \tag{1}$$
$$R_{EN} = (r^2 + s^2)^{0.5}. \tag{2}$$

The degree to which the projection of the GCPs varies over time is assessed by examining the relative changes in the GCP projection locations (m) between the beginning and end of the feature tracking process:

$$[u_{EN}, v_{EN}] = [(r_{n+9} - r_n), (s_{n+9} - s_n)], \tag{3}$$
$$U_{EN} = (u_{EN}^2 + v_{EN}^2)^{0.5}. \tag{4}$$

Two-dimensional natural neighbour interpolation of the GCP errors is performed, giving spatially distributed estimates of R_{EN} and U_{EN} (Fig. 1, Sect. 2.4).

2.5 Surface velocity calculation

As with the GCPs, between the nth and $n + 9$th frames, surface water features are defined and tracked using the KLT algorithm, with their start and finish positions being stored in pixel units. During this process, features were only tracked if they were within the central 90 % of the image. This was necessary to minimize the potential for residual distortion effects to bias measurements, as these were most likely to persist close to the image boundaries (Detert and Weitbrecht, 2015). The start and finish positions (px) of selected surface water features are converted to real-world start and finish co-ordinates, i.e. $[X_n, Y_n]$ and $[X_{n+9}, Y_{n+9}]$ respectively. This is again achieved through two-dimensional transformation (Fujita and Kunita, 2011; Fujita et al., 1998), based on the optimized camera models specific to the nth and $n + 9$th frames (Messerli and Grinsted, 2015). This method is analogous to the vector correction method (Fujita and Kunita, 2011) whereby stationary objects yield zero or negligible velocity values, with the movement of surface water velocity vectors being corrected for background image displacement. This process enables the calculation of two-dimensional velocities $[u, v]$ following application of a conversion factor k to account for the number of tracked frames I and seconds per frame F:

$$[\Delta X \, \Delta Y] = \left[X_{n+9}, Y_{n+9}, \right] - [X_n, Y_n], \tag{5}$$

$$k = \frac{1}{(F \, I)}, \tag{6}$$

$$[u, v] = [\Delta X, \Delta Y][k], \tag{7}$$

from which the velocity magnitude is obtained:

$$U = \sqrt{u^2 + v^2}. \tag{8}$$

Velocity (U) measurements in areas defined as having poor transformation accuracy (i.e. $R_{EN} \geq 1\,\mathrm{m}$), or significant apparent movement of the GCPs between frames (i.e. $U_{EN} \geq 0.3\,\mathrm{m}$), are removed prior to analysis, in addition to tracked features exhibiting minimal displacement (i.e. $U \leq 0.3\,\mathrm{m}$). This resulted in 48 % of the original surface water features being eliminated (Fig. 1, Sect. 2.5).

3 Results

3.1 Camera motion

Using the 20 000 potential solutions, the optimized master camera model was selected based on the minimum square projection error of the GCPs (RMSE – root-mean-square error). The minimum RMSE of the 20 000 solutions was 11.4 px ($n = 8$). Optimization of the initial camera model took 25 min (3.2 GHz CPU, 8 GB RAM) and accounted for 29 % of the total processing time. Following perturbation of geographical and orientation parameters for each frame, the

Table 1. Optimized parameters of the distorted camera models.

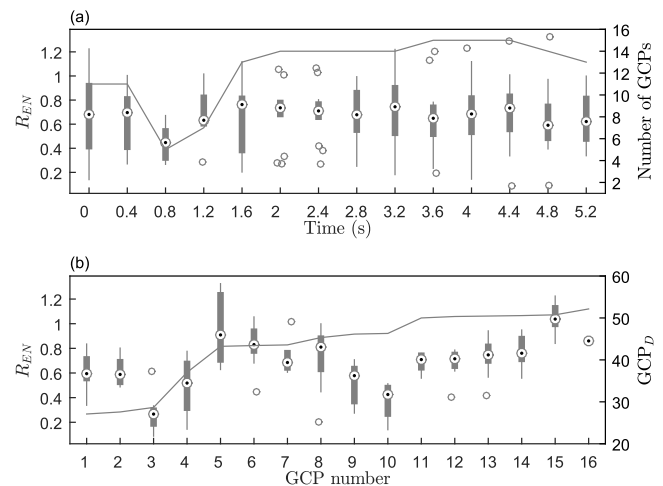| Optimized parameter	Frame number	
	1	140
X (m)	324566.9	324565.8
Y (m)	748589.7	748591.3
Z (m)	15.2	16.4
Yaw (radians)	0.33	−0.14
Pitch (radians)	0.61	0.67
Roll (radians)	0.02	0.08
RMSE (px)	11.4	8.3

Figure 2. Box plots showing how projection residuals R_{EN} (m) of all GCPs vary with **(a)** time and **(b)** distance from the UAV camera. Dot within circle: median; box: 25th and 75th percentiles; whiskers: extremes; open circle: outliers. Line: number of GCPs/distance of GCP from image source (m).

flight path of the UAV was successfully modelled (Fig. 1, Sect. 2.3). The cumulative Euclidean distance travelled by the UAV over the 140 frames was 13.2 m (mean velocity = 2.5 m s^{-1}), whilst the camera rotated on the y axis by 28° (Table 1). During the video the RMSE of the optimized camera did not exceed 12.9 px, with a mean μ of 9.6 px and a standard deviation σ of 1.3 px.

3.2 Positional accuracy

Analysis indicates that the precision of the geometric projection R_{EN} remains relatively stable throughout the video (Fig. 2a). However, the number of GCPs does exert some influence on the associated R_{EN} value. The minimum R_{EN} value of 0.4 m is observed at 0.8 s, when six GCPs are within shot. With the removal of GCPs that are difficult to resolve, located close to the upper edge of the frame, R_{EN} naturally decreases. The maximum R_{EN} value is 0.76 m, which occurs at 1.6 s (13 GCPs). This provides an indication of the minimum spatial scale over which measurements should be
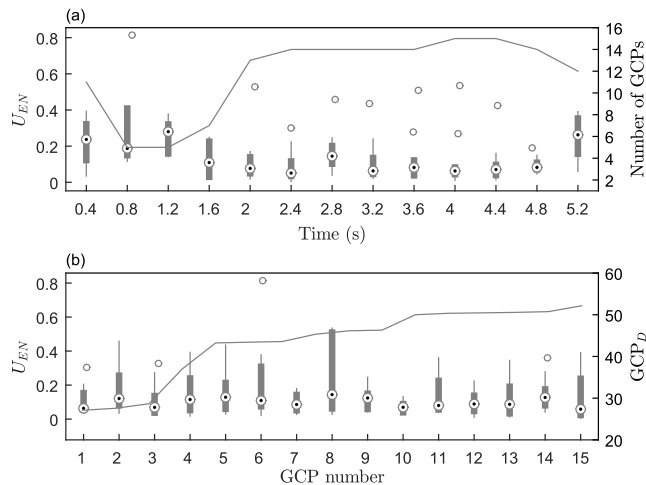
Figure 3. Box plots showing how the apparent movement U_{EN} (m) of all GCPs varies with **(a)** time and **(b)** distance from the UAV camera. Dot within circle: median; box: 25th and 75th percentiles; whiskers: extremes; open circle: outliers. Line: number of GCPs/distance of GCP from image source (m).

averaged and reported. Significant spatial variability in R_{EN} values is observed, with median individual GCP R_{EN} values ranging from 0.27 to 1.0 m (Fig. 2b). However, the interquartile range of R_{EN} for each GCP is relatively small, with a median value of 0.15 m. Furthermore, due to the lack of correlation between geolocation errors and the distance of the GCP from the camera source, we eliminate the potential for significant errors being a function of reduced pixel density per unit area as GCP distance increases (Fig. 2b). These findings indicate that the geo-registration errors are relatively stable and occur as a result of persistent residual distortion effects following image correction, especially close to the image boundaries, due to the specified transformation parameters being sub-optimal.

Whilst accurate geometric projection is essential for observed velocities to be assigned an appropriate spatial reference, the precision of the transformation over time is of greatest importance. Unacceptable apparent ground velocities as a result of unstable transformation over time would undermine the value of tracking surface features. This error U_{EN} is quantified by computing the relative movement of reference features across each tracking interval. Unaccounted for movement generally decreases over time, following the maximum U_{EN} of 0.28 m at 1.2 s through to the minimum of 0.05 m at 2.4 s (Fig. 3a). Median U_{EN} values continue to be < 0.15 m throughout the sequence until the final frame when median U_{EN} increases to 0.26 m. Unlike the spatial variability of R_{EN} values, U_{EN} values for specific GCPs are observed to be relatively consistent (Fig. 3b). The median of the 15 GCPs ranges from 0.05 to 0.13 m, with no apparent relationship between the distance of the GCP and U_{EN}. These findings illustrate the relative spatial and temporal stability of the geometric

transformation. Occasionally however the apparent velocity of fixed targets, and therefore the associated error, is significant (i.e. > 0.3 m). In these instances, features tracked within areas of unaccounted for movement are identified and filtered from subsequent analysis (Fig. 1, Sect. 2.4).

3.3 Feature tracking and velocity estimation

Following the analysis of the 5.2 s video, and the filtering of features tracked from within inaccurately projected regions of the image, a total of 2644 velocity vectors were compiled within a 624 m^2 area of the Alyth Burn and the surrounding inundated landscape (Fig. 4). This results in an average of 4.2 at a rate of 508 measurements s^{-1}. Analysis of these vectors provides an insight into the complexity of interactions between flow, sediment load, and debris during flash floods. The bridge in the video (which was ultimately destroyed) was recorded in the imagery as being blocked by coarse woody debris (see Supplement). Due to the turbulent vortices generated by this blockage, surface velocities upstream of the bridge are calculated to be minimal (0.3–0.4 m s^{-1}). This blockage reduced conveyance of the flood waters, with a proportion of channel flow becoming diverted into the adjacent street where surface velocities exceeded 1.2 m s^{-1} (Fig. 4). Similar breaches of the river defences upstream of the camera frame result in the routing of flood waters along the adjacent street. This routing produces velocities in the region of 0.9 m s^{-1} before these waters are mixed with those diverted from the main channel at the bridge within the camera shot. Further along the road, flow is disrupted by a partially submerged vehicle. This again results in the visible deflection of flow. In the main channel, immediately downstream of the bridge, large-scale turbulent structures as a result of secondary circulation are detected, with surface velocities progressively increasing to a maximum of 2.14 m s^{-1} (Fig. 4). The uncertainty attached to all calculated velocities is relatively low, with a spatial average across the area of ± 0.15 m s^{-1}. Little difference is observed in the uncertainty attached to out-of-bank velocities (± 0.15 m s^{-1}) and within-channel velocities (± 0.16 m s^{-1}), illustrating the consistency of the approach.

4 Discussion

4.1 Adoption of feature tracking approach

Application of feature tracking in open channels is dominated by methods operating in the Eulerian frame of reference (e.g. LSPIV). These methods have been widely successful in the characterization of instantaneous and time-averaged velocities for the determination of flood discharges, with deviations from acoustically derived measurements of < 10 % (Jodeau et al., 2008; Muste et al., 2008; Dramais et al., 2011). Measurements made in the Lagrangian frame of reference (e.g. LSPTV), where the paths of individual parti-
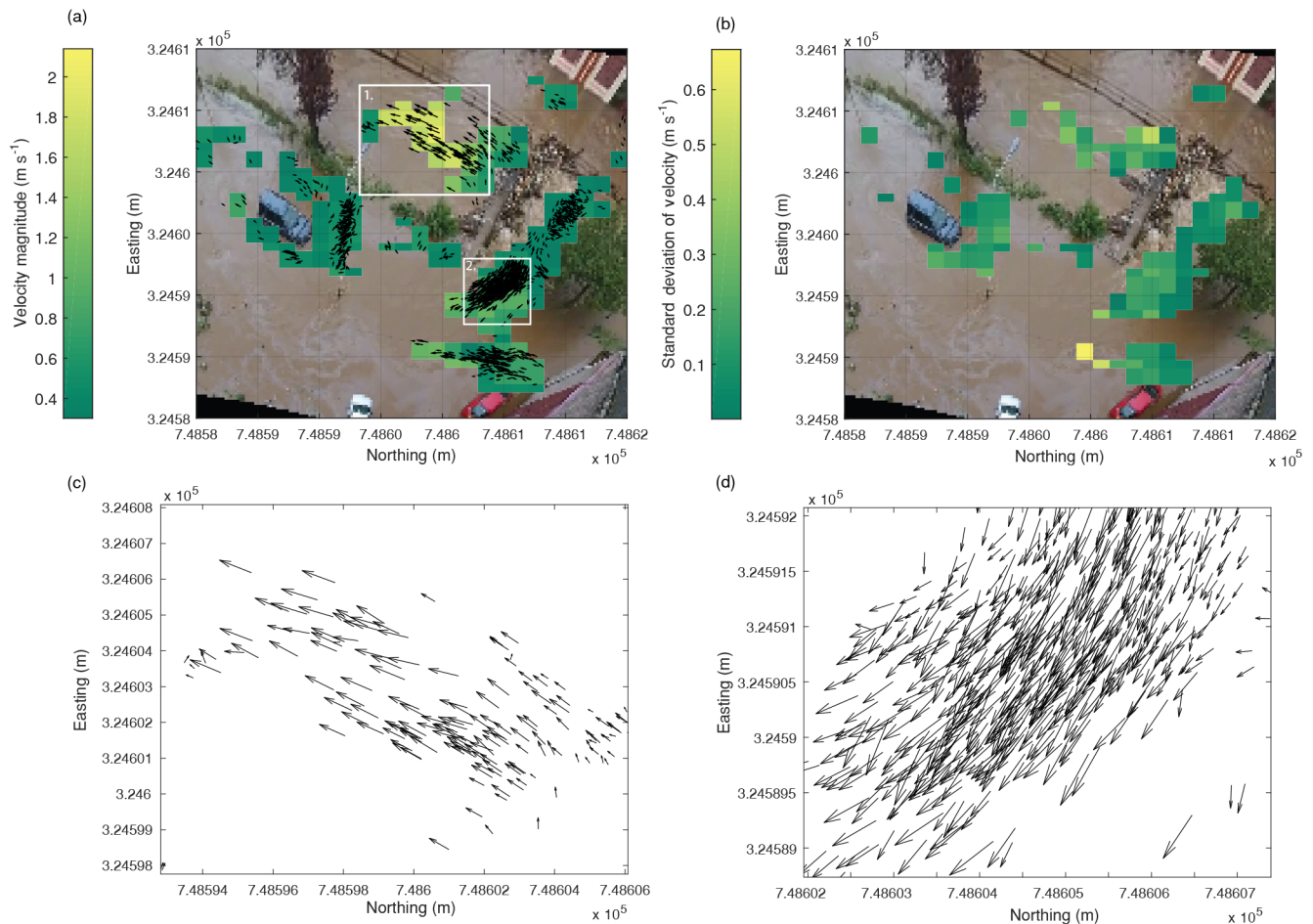
Figure 4. Images showing **(a)** velocity magnitude and **(b)** standard deviation of measurements calculated by tracking optically visual surface features. Zoomed-in views of velocity vectors are provided in **(c)** and **(d)**, which correspond to the boxes labelled 1 and 2 respectively in **(a)**.

cles are assessed, have been less widely adopted for monitoring high-magnitude events. This is despite LSPTV replicating hydraulics accurately with improved performance close to boundaries and in areas experiencing high velocity gradients (Admiraal et al., 2004). Enhanced spatial resolution of measurements may also be possible with lower seeding densities (Detert and Weitbrecht, 2015). Our implementation of the KLT algorithm has demonstrated its potential to generate large volumes of temporally consistent data at a distance of up to 50 m. However, feature tracking from non-stationary platforms poses additional challenges in accounting for errors related to sensor movement and orientation. These challenges, which must be addressed for this approach to be beneficial for monitoring flood flows, are discussed in the following sections.

4.2 Transformation errors

Transformation from pixel to world co-ordinates is one of the greatest challenges in generating accurate velocity estimates, even when measurements are conducted in controlled conditions from sensors of known, fixed locations (Lewis and Rhoads, 2015). Specific error associated with rectification can be controlled by ensuring the camera lens is (i) orthogonal to the water surface (e.g. Lewis and Rhoads, 2015); (ii) corrected for distortion (e.g. Le Boursicaud et al., 2015); and (iii) accurately calibrated using stable GCPs throughout the field-of-view (e.g. Dramais et al., 2011). Unfortunately it is not always possible to maintain the camera lens orthogonal to the water surface whilst capturing flow processes at the scale of interest, which often necessitates oblique image capture. Such oblique image capture may pose methodological difficulties due to far-field objects being poorly resolved relative to those in near-field. Secondly, lens distortion must be removed prior to the implementation of traditional plan-to-plan perspective projection (Le Boursicaud et al., 2015). This can be achieved based on the manufacturer's specifications (e.g. Detert and Weitbrecht, 2015), or through manual calibration (e.g. Tauro et al., 2015a); however, residual distortion may persist close to image boundaries. Finally, following internal camera calibration, the success of the trans-

formation depends on the three-dimensional distribution of GCPs. Distribution of at least four GCPs is required for a two-dimensional transformation (Fujita et al., 1998; Fujita and Kunita, 2011), or a minimum of six GCPs distributed across the region of interest for a three-dimensional plan-to-plan perspective projection (Jodeau et al., 2008; Muste et al., 2008). For accurate transformation, elevation errors can be minimized by ensuring GCPs are similar to or located parallel to the water surface elevation (Jodeau et al., 2008; Fujita and Kunita, 2011). However, an implicit assumption of this approach is that the planar free surface is horizontal and that free-surface undulations are negligible across the frame. Due to the often negligible water surface slopes across the area of interest, errors are typically assumed to be insignificant (Hauet et al., 2008), with previous research indicating that water level errors of ± 0.3 m result in velocity deviations of $< \pm 5\%$ (Le Boursicaud et al., 2015). A second source of elevation error may be induced by local water level variability as a result of standing waves created by hydraulic jumps, or obstacles. However, previous research (e.g. Dramais et al., 2011) has demonstrated that local variability of up to 1 m may still have an insignificant impact on stream-wise velocity measurements when images are collected perpendicular to flow.

4.3   Accounting for movement

In addition to oblique image capture, camera motion can greatly diminish the precision of any calibration and transformation process. In the case of monitoring fluvial flash floods from UAV platforms, camera motion is inevitable (Tauro et al., 2015a, b), and this movement should be corrected for on a frame-by-frame basis. This may be achieved through the utilization of on-board GPS systems (e.g. Bolognesi et al., 2016) or fixed reference points (e.g. Lewis and Rhoads, 2015). In the approach reported on here, we adopt a methodology to account for these uncertainties and their impacts on subsequent velocity measurements whereby fixed control points are manually selected and automatically tracked between frames using the KLT algorithm. Automatic tracking of GCPs is enabled by the distinct image textures of the water surface and the built environment, enabling the precision of the rectification process to be quantified and uncertainty in velocity measurements to be established. Whilst this procedure requires some supervision, in future deployments, purpose-built GCPs will be installed across the area of interest with distinct optical characteristics so that (semi-)automatic registration would be possible. However, in areas where naturally existing GCP features do not exist, or where installation of purpose-built GCPs would be problematic, a different approach would be required. Therefore, future research should seek to assess the potential for on-board GPS systems, ranging tools (e.g. lasers), and calibrated cameras to enable UAVs to be utilized. This will also open up the possibility of real-time capture of hydraulic properties of flow.

Due to the responsive nature of this survey of the July 2015 Alyth flood event, the distribution of GCPs was not pre-determined, so despite a total of 15 linear structures within the urban landscape that intersected the water surface being identified as GCPs, spatial coverage is incomplete and availability is temporally variable. While rapid response deployment of UAVs during floods may therefore introduce errors in the projection that would otherwise be accounted for in planned deployments, the majority of surveys at high discharge will naturally be "unplanned" and the result of rapid field deployment. Despite this, and the technical challenges of flying surveys during periods of heavy rainfall associated with floods, the relatively stable transformations achieved throughout the duration of the July 2015 Alyth video presented here demonstrate the utility of the approach.

5   Conclusions

UAVs have the potential to capture information about dynamics at the earth's surface in hazardous and previously inaccessible locations. Highly transient and oft-immeasurable hydraulic phenomena may be quantified at previously unattainable spatial and temporal resolutions using image acquisition of flash floods and subsequent object-based analysis. The potential for this approach to provide valuable information about the hydraulic conditions present during dynamic, high-energy flash floods has until now not been explored.

This paper adopts a novel approach, utilizing the KLT algorithm to track features present on the water surface which are related to the free-surface velocity. Following the successful tracking of features, a method analogous to the vector correction method has enabled accurate geometric rectification of velocity vectors. We subsequently explored uncertainties associated with the rectification process induced by unsteady camera movements. The maximum geolocation error is 1.0 m, which provides an indication of the minimum spatial scale over which measurements should be averaged and reported. Significant spatial variability in geo-registration error values is observed, with median individual GCP error values ranging from 0.27 to 1.0 m. Our analysis eliminates the potential for significant errors being a function of reduced pixel density per unit area as GCP distance increases. Geo-registration errors are relatively stable and occur as a result of persistent residual distortion effects following image correction, especially close to the image boundaries, due to the specified transformation parameters being sub-optimal. Future approaches should seek to use a camera with minimal lens distortion, for which the internal properties of the camera are calibrated, rather than adopting manufacturer lens specifications. The apparent ground velocities of the 15 GCPs range from 0.05 to 0.13 m, with no apparent relationship between the distance of the GCP and observed

ground velocity. These findings illustrate the relative spatial and temporal stability of the geometric transformation.

The application of this approach to assess the hydraulic conditions present in the Alyth Burn during a 1 : 200 year flash flood (Perth and Kinross Council et al., 2015) resulted in the generation of an average 4.2 at a rate of 508 measurements s^{-1}. Analysis of these vectors provided a rare insight into the complexity of channel–overbank interactions during flash floods. The uncertainty attached to the calculated velocities is relatively low, with a spatial average across the area of $\pm 0.15\,m\,s^{-1}$. Within-channel and overbank uncertainty in velocity estimates is comparable.

Comprehensive and innovative monitoring programmes (e.g. Ip et al., 2006; Quevauviller et al., 2012; Smith et al., 2014) have previously improved understanding of transient, rate limiting processes and catchment dynamics during extreme flash floods (Zanon et al., 2010), Similarly, we anticipate that this methodology will be of great use in quantifying highly transient flood flows within ungauged rivers across a wide range of fluvial environments.

6 Data availability

Datasets utilized in the production of this research article are available for download in the Supplement.

The Supplement related to this article is available online at doi:10.5194/hess-20-4005-2016-supplement.

References

Admiraal, D. M., Stansbury, J. S., and Haberman, C. J.: Case study: Particle velocimetry in a model of lake Ogallala, J. Hydraul. Eng., 130, 599–607, 2004.

Beniston, M.: Trends in joint quantiles of temperature and precipitation in Europe since 1901 and projected for 2100, Geophys. Res. Lett., 36, L07707, doi:10.1029/2008GL037119, 2009.

Bolognesi, M., Farina, G., Alvisi, S., Franchini, M., Pellegrinelli, A., and Russo, P.: Measurement of surface velocity in open channels using a lightweight remotely piloted aircraft system, Geomatics, Natural Hazards and Risk, 1–14, doi:10.1080/19475705.2016.1184717, 2016.

Borga, M., Gaume, E., Creutin, J. D., and Marchi, L.: Surveying flash floods: gauging the ungauged extremes, Hydrol. Process., 22, 3883–3885, doi:10.1002/hyp.7111, 2008.

Bracken, L. J. and Croke, J.: The concept of hydrological connectivity and its contribution to understanding runoff-dominated geomorphic systems, Hydrol. Process., 21, 1749–1763, doi:10.1002/hyp.6313, 2007.

Braud, I., Ayral, P.-A., Bouvier, C., Branger, F., Delrieu, G., Le Coz, J., Nord, G., Vandervaere, J.-P., Anquetin, S., Adamovic, M., Andrieu, J., Batiot, C., Boudevillain, B., Brunet, P., Carreau, J., Confoland, A., Didon-Lescot, J.-F., Domergue, J.-M., Douvinet, J., Dramais, G., Freydier, R., Gérard, S., Huza, J., Leblois, E., Le Bourgeois, O., Le Boursicaud, R., Marchand, P., Martin, P., Nottale, L., Patris, N., Renard, B., Seidel, J.-L., Taupin, J.-D., Vannier, O., Vincendon, B., and Wijbrans, A.: Multi-scale hydrometeorological observation and modelling for flash flood understanding, Hydrol. Earth Syst. Sci., 18, 3733–3761, doi:10.5194/hess-18-3733-2014, 2014.

Chen, W. and Mied, R. P.: River velocities from sequential multi-spectral remote sensing images, Water Resour. Res., 49, 3093–3103, doi:10.1002/wrcr.20267, 2013.

CloudCompare: Version 2.6.1, EDF R&D, GPL software, Telecom ParisTech, http://www.cloudcompare.org/ last access: 6 May 2015.

Detert, M. and Weitbrecht, V.: A low-cost airborne velocimetry system: proof of concept, J. Hydraul. Res., 53, 532–539, doi:10.1080/00221686.2015.1054322, 2015.

Doocy, S., Daniels, A., Murray, S., and Kirsch, T. D.: The Human Impact of Floods: a Historical Review of Events 1980–2009 and Systematic Literature Review, PLoS Currents, 5, doi:10.1371/currents.dis.f4deb457904936b07c09daa98ee8171a, 2013.

Dramais, G., Le Coz, J., Camenen, B., and Hauet, A.: Advantages of a mobile LSPIV method for measuring flood discharges and improving stage–discharge curves, Journal of Hydro-environment Research, 5, 301–312, doi:10.1016/j.jher.2010.12.005, 2011.

Fekete, B. M., Robarts, R. D., Kumagai, M., Nachtnebel, H.-P., Odada, E., and Zhulidov, A. V.: Time for in situ renaissance, Science, 349, 685–686, doi:10.1126/science.aac7358, 2015.

Fletcher, R.: Modified Marquardt subroutine for non-linear least squares, Atomic Energy Research Establishment, Harwell (England), Harwell, UK, 1971.

Fujita, I. and Kunita, Y.: Application of aerial LSPIV to the 2002 flood of the Yodo River using a helicopter mounted high density video camera, Journal of Hydro-environment Research, 5, 323–331, doi:10.1016/j.jher.2011.05.003, 2011.

Fujita, I., Muste, M., and Kruger, A.: Large-scale particle image velocimetry for flow analysis in hydraulic engineering applications, J. Hydraul. Res., 36, 397–414, doi:10.1080/00221689809498626, 1998.

Garambois, P. A., Larnier, K., Roux, H., Labat, D., and Dartus, D.: Analysis of flash flood-triggering rainfall for a process-oriented hydrological model, Atmos. Res., 137, 14–24, doi:10.1016/j.atmosres.2013.09.016, 2014.

Gaume, E. and Borga, M.: Post-flood field investigations in upland catchments after major flash floods: proposal of a methodology and illustrations, J. Flood Risk Management, 1, 175–189, doi:10.1111/j.1753-318X.2008.00023.x, 2008.

Hauet, A., Kruger, A., Krajewski, W. F., Bradley, A., Muste, M., Creutin, J.-D., and Wilson, M.: Experimental system for real-time discharge estimation using an image-based method, J. Hydrol. Eng., 13, 105–110, 2008.

Ip, F., Dohm, J. M., Baker, V. R., Doggett, T., Davies, A. G., Castaño, R., Chien, S., Cichy, B., Greeley, R., Sherwood, R., Tran, D., and Rabideau, G.: Flood detection and monitoring with the Autonomous Sciencecraft Experiment onboard EO-1, Remote Sens. Environ., 101, 463–481, doi:10.1016/j.rse.2005.12.018, 2006.

Jodeau, M., Hauet, A., Paquier, A., Le Coz, J., and Dramais, G.: Application and evaluation of LS-PIV technique for the monitoring of river surface velocities in high flow conditions, Flow Measurement and Instrumentation, 19, 117–127, doi:10.1016/j.flowmeasinst.2007.11.004, 2008.

Kääb, A. and Leprince, S.: Motion detection using near-simultaneous satellite acquisitions, Remote Sens. Environ., 154, 164–179, doi:10.1016/j.rse.2014.08.015, 2014.

Kantoush, S. A., De Cesare, G., Boillat, J. L., and Schleiss, A. J.: Flow field investigation in a rectangular shallow reservoir using UVP, LSPIV and numerical modelling, Flow Measurement and Instrumentation, 19, 139–144, doi:10.1016/j.flowmeasinst.2007.09.005, 2008.

Kim, Y., Muste, M., Hauet, A., Krajewski, W. F., Kruger, A., and Bradley, A.: Stream discharge using mobile large-scale particle image velocimetry: A proof of concept, Water Resour. Res., 44, W09502, doi:10.1029/2006WR005441, 2008.

Le Boursicaud, R., Pénard, L., Hauet, A., Thollet, F., and Le Coz, J.: Gauging extreme floods on YouTube: application of LSPIV to home movies for the post-event determination of stream discharges, Hydrol. Process., 30, 90–105, doi:10.1002/hyp.10532, 2015.

Le Coz, J., Hauet, A., Pierrefeu, G., Dramais, G., and Camenen, B.: Performance of image-based velocimetry (LSPIV) applied to flash-flood discharge measurements in Mediterranean rivers, J. Hydrol., 394, 42–52, doi:10.1016/j.jhydrol.2010.05.049, 2010.

Lewis, Q. W. and Rhoads, B. L.: Resolving two-dimensional flow structure in rivers using large-scale particle image velocimetry: An example from a stream confluence, Water Resour. Res., 51, 7977–7994, doi:10.1002/2015WR017783, 2015.

Liu, G., Schwartz, F. W., Tseng, K.-H., and Shum, C. K.: Discharge and water-depth estimates for ungauged rivers: Combining hydrologic, hydraulic, and inverse modeling with stage and water-area measurements from satellites, Water Resour. Res., 51, 6017–6035, doi:10.1002/2015WR016971, 2015.

Martinis, S., Twele, A., and Voigt, S.: Towards operational near real-time flood detection using a split-based automatic thresholding procedure on high resolution TerraSAR-X data, Nat. Hazards Earth Syst. Sci., 9, 303–314, doi:10.5194/nhess-9-303-2009, 2009.

Mason, D. C., Cobby, D. M., Horritt, M. S., and Bates, P. D.: Floodplain friction parameterization in two-dimensional river flood models using vegetation heights derived from airborne scanning laser altimetry, Hydrol. Process., 17, 1711–1732, doi:10.1002/hyp.1270, 2003.

Mayes, W. M., Walsh, C. L., Bathurst, J. C., Kilsby, C. G., Quinn, P. F., Wilkinson, M. E., Daugherty, A. J., and O'Connell, P. E.: Monitoring a flood event in a densely instrumented catchment, the Upper Eden, Cumbria, UK, Water Environ. J., 20, 217–226, doi:10.1111/j.1747-6593.2005.00006.x, 2006.

Messerli, A. and Grinsted, A.: Image georectification and feature tracking toolbox: ImGRAFT, Geoscientific Instrumentation, Methods and Data Systems, 4, 23–34, 2015.

Milner, A. M., Robertson, A. L., McDermott, M. J., Klaar, M. J., and Brown, L. E.: Major flood disturbance alters river ecosystem evolution, Nature Climate Change, 3, 137–141, 2013.

Muste, M., Fujita, I., and Hauet, A.: Large-scale particle image velocimetry for measurements in riverine environments, Water Resour. Res., 44, W00D19, doi:10.1029/2008WR006950, 2008.

Niethammer, U., James, M. R., Rothmund, S., Travelletti, J., and Joswig, M.: UAV-based remote sensing of the Super-Sauze landslide: Evaluation and results, Eng. Geol., 128, 2–11, doi:10.1016/j.enggeo.2011.03.012, 2012.

Pagano, C., Tauro, F., Grimaldi, S., and Porfiri, M.: Development and Testing of an Unmanned Aerial Vehicle for Large Scale Particle Image Velocimetry, ASME 2014 Dynamic Systems and Control Conference, V003T044A001-V003T044A001, 2014.

Patalano, A., Garcia, C. M., Brevis, W., Bleninger, T., Guillen, N., Moreno, L., and Rodriguez, A.: Recent advances in eulerian and lagragian large-scale particle image velocimetry, E-proceedings of the 36th IAHR World Congress, The Hauge, Netherlands, 2015.

Pentari, A., Moirogiorgou, K., Livanos, G., Iliopoulou, D., and Zervakis, M.: Feature analysis on river flow video data for floating tracers detection, 2014 IEEE International Conference on Imaging Systems and Techniques (IST), 287–292, 2014.

Perth and Kinross Council: The Scottish Environment Protection Agency, and Scottish Natural Heritage: Joint Agency Report on the Flooding in Alyth of 17 July 2015, http://www.pkc.gov.uk/CHttpHandler.ashx?id=33291&p=0 (last access: 6 January 2016), 2015.

Puleo, J. A., McKenna, T. E., Holland, K. T., and Calantoni, J.: Quantifying riverine surface currents from time sequences of thermal infrared imagery, Water Resour.Res., 48, W01527, doi:10.1029/2011WR010770, 2012.

Quevauviller, P., Barceló, D., Beniston, M., Djordjevic, S., Harding, R. J., Iglesias, A., Ludwig, R., Navarra, A., Navarro Ortega, A., Mark, O., Roson, R., Sempere, D., Stoffel, M., van Lanen, H. A. J., and Werner, M.: Integration of research advances in modelling and monitoring in support of WFD river basin management planning in the context of climate change, Sci. Total Environ., 440, 167–177, doi:10.1016/j.scitotenv.2012.07.055, 2012.

Quinn, P. F. and Beven, K. J.: Spatial and temporal predictions of soil moisture dynamics, runoff, variable source areas and evapotranspiration for plynlimon, mid-wales, Hydrol. Process., 7, 425–448, doi:10.1002/hyp.3360070407, 1993.

Refice, A., Capolongo, D., Pasquariello, G., D'Addabbo, A., Bovenga, F., Nutricato, R., Lovergine, F. P., and Pietranera, L.: SAR and InSAR for Flood Monitoring: Examples With COSMO-SkyMed Data, IEEE J. Sel. Top. Appl., 7, 2711–2722, doi:10.1109/JSTARS.2014.2305165, 2014.

Rojas, R., Feyen, L., Bianchi, A., and Dosio, A.: Assessment of future flood hazard in Europe using a large ensemble of bias-corrected regional climate simulations, J. Geophys. Res.-Atmos., 117, D17109, doi:10.1029/2012JD017461, 2012.

Ryan, J. C., Hubbard, A. L., Box, J. E., Todd, J., Christoffersen, P., Carr, J. R., Holt, T. O., and Snooke, N.: UAV photogram-

metry and structure from motion to assess calving dynamics at Store Glacier, a large outlet draining the Greenland ice sheet, The Cryosphere, 9, 1–11, doi:10.5194/tc-9-1-2015, 2015.

Sangati, M., Borga, M., Rabuffetti, D., and Bechini, R.: Influence of rainfall and soil properties spatial aggregation on extreme flash flood response modelling: An evaluation based on the Sesia river basin, North Western Italy, Adv. Water Resour., 32, 1090–1106, doi:10.1016/j.advwatres.2008.12.007, 2009.

Schumann, G., Matgen, P., Hoffmann, L., Hostache, R., Pappenberger, F., and Pfister, L.: Deriving distributed roughness values from satellite radar data for flood inundation modelling, J. Hydrol., 344, 96–111, doi:10.1016/j.jhydrol.2007.06.024, 2007.

Shi, J. and Tomasi, C.: Good features to track, 1994 IEEE Computer Society Conference on Computer Vision and Pattern Recognition, 593–600, 1994.

Simeonov, J. A., Holland, K. T., Calantoni, J., and Anderson, S. P.: Calibrating discharge, bed friction, and datum bias in hydraulic models using water level and surface current observations, Water Resour. Res., 49, 8026–8038, doi:10.1002/2013WR014474, 2013.

Smith, M. W., Carrivick, J. L., Hooke, J., and Kirkby, M. J.: Reconstructing flash flood magnitudes using "Structure-from-Motion": A rapid assessment tool, J. Hydrol., 519, 1914–1927, doi:10.1016/j.jhydrol.2014.09.078, 2014.

Soulsby, C., Malcolm, R., Helliwell, R., Ferrier, R. C., and Jenkins, A.: Isotope hydrology of the Allt a' Mharcaidh catchment, Cairngorms, Scotland: implications for hydrological pathways and residence times, Hydrol. Process., 14, 747–762, 2000.

Soulsby, C., Neal, C., Laudon, H., Burns, D. A., Merot, P., Bonell, M., Dunn, S. M., and Tetzlaff, D.: Catchment data for process conceptualization: simply not enough?, Hydrol. Process., 22, 2057–2061, doi:10.1002/hyp.7068, 2008.

Sun, X., Shiono, K., Chandler, J. H., Rameshwaran, P., Sellin, R. H. J., and Fujita, I.: Discharge estimation in small irregular river using LSPIV, Proceedings of the ICE-Water Management, 163, 247–254, 2010.

Tauro, F., Pagano, C., Phamduy, P., Grimaldi, S., and Porfiri, M.: Large-Scale Particle Image Velocimetry From an Unmanned Aerial Vehicle, IEEE/ASME Transactions on Mechatronics, 20, 3269–3275, doi:10.1109/TMECH.2015.2408112, 2015a.

Tauro, F., Petroselli, A., and Arcangeletti, E.: Assessment of drone-based surface flow observations, Hydrol. Process., 30, 1114–1130, doi:10.1002/hyp.10698, 2015b.

Wong, J. S., Freer, J. E., Bates, P. D., Sear, D. A., and Stephens, E. M.: Sensitivity of a hydraulic model to channel erosion uncertainty during extreme flooding, Hydrol. Process., 29, 261–279, doi:10.1002/hyp.10148, 2015.

Wright, N., Villanueva, I., Bates, P., Mason, D., Wilson, M., Pender, G., and Neelz, S.: Case Study of the Use of Remotely Sensed Data for Modeling Flood Inundation on the River Severn, UK, J. Hydraul. Eng., 134, 533–540, doi:10.1061/(ASCE)0733-9429(2008)134:5(533), 2008.

Zanon, F., Borga, M., Zoccatelli, D., Marchi, L., Gaume, E., Bonnifait, L., and Delrieu, G.: Hydrological analysis of a flash flood across a climatic and geologic gradient: The September 18, 2007 event in Western Slovenia, J. Hydrol., 394, 182–197, doi:10.1016/j.jhydrol.2010.08.020, 2010.